ELSEVIER

Contents lists available at ScienceDirect

## **Extreme Mechanics Letters**

journal homepage: www.elsevier.com/locate/eml



# Atomistic simulations of superplasticity and amorphization of nanocrystalline anatase TiO<sub>2</sub>



Xuan Zhang<sup>a</sup>, Huajian Gao<sup>b</sup>, Xiaoyan Li<sup>a,\*</sup>

- <sup>a</sup> Center for Advanced Mechanics and Materials, Applied Mechanics Laboratory, Department of Engineering Mechanics, Tsinghua University, Beijing 100084. China
- <sup>b</sup> School of Engineering, Brown University, Providence, RI 02912, USA

#### HIGHLIGHTS

- Reveal the underlying deformation mechanisms of nanocrystalline anatase.
- Demonstrate the tensile superplasticity and good compressibility of nanocrystalline anatase.
- Show the amorphization induced by high compressive stress in nanocrystalline anatase.

#### ARTICLE INFO

#### Article history: Received 29 March 2018 Received in revised form 30 May 2018 Accepted 31 May 2018 Available online 4 June 2018

Keywords: Nanocrystalline TiO<sub>2</sub> Superplasticity Amorphization Atomistic simulation

#### ABSTRACT

As an important type of functional material, nanocrystalline TiO<sub>2</sub> with anatase phase has been used for solar energy conversion and photocatalysis. However, there have been only a few limited studies on the mechanical behaviors of nanocrystalline anatase. We performed a series of large-scale atomistic simulations to investigate the deformation of nanocrystalline anatase with mean grain sizes varying from 2 nm to 6 nm and amorphous TiO<sub>2</sub> under uniaxial tension and compression at room temperature. The simulation results showed that for uniaxial tension, the fracture strains of simulated samples increase as the mean grain size decreases, and a superplastic deformation occurred in the nanocrystalline sample with a grain size of 2 nm. Such superplasticity of nanocrystalline anatase is attributed to the dominance of grain boundary sliding and nanoscale cavitation during deformation. The simulation results also showed that during uniaxial compression, the amorphization induced by high local compressive stress is the controlling plastic deformation mechanism, resulting in a good compressibility of nanocrystalline TiO<sub>2</sub>. During both tension and compression, nanocrystalline TiO<sub>2</sub> exhibited good deformability, which is attributed to the fact that the grain boundaries with high volume fractions and disordered structures accommodated large plastic strains. Our present study provides a fundamental understanding of the plastic deformation of nanocrystalline anatase TiO2, as well as a route for enhancing the tensile and compressive deformability of nanostructured ceramics.

© 2018 Elsevier Ltd. All rights reserved.

#### 1. Introduction

As an important functional semiconductor, titanium dioxide (TiO<sub>2</sub>) has broad applications in photovoltaics, photocatalysis, memristors, optical coatings and mixed conductors [1,2]. However, like typical inorganic ceramics, coarse-grained TiO<sub>2</sub> is intrinsically brittle, restricting its practical applications. It has been recognized that the refinement of the grains of polycrystalline ceramics to several microns and even smaller scales tends to significantly increase their ductility [3–11]. In particular, when the grain size

of polycrystalline ceramics is reduced to a few nanometers, the intrinsically brittle ceramics became ductile and are able to sustain a large plastic deformation strain of approximately 100% at temperatures of approximately 200 °C [3], indicating superplastic behavior. Therefore, to avoid the intrinsic brittleness, various nanocrystalline TiO<sub>2</sub> materials have been synthesized. TiO<sub>2</sub> nanowires/nanofibers with anatase phase have been successfully fabricated through electrospinning or blow-spinning [12,13]. The diameters of these TiO<sub>2</sub> nanowires/nanofibers could be controlled in the range from 20 to 200 nm [12], enabling a grain size of tens of nanometers. Nanocrystalline TiO<sub>2</sub> films have also been manufactured by compressing TiO<sub>2</sub> nanoparticles at room temperature or high temperatures and combining some chemical processes [12,13]. These nanocrystalline TiO<sub>2</sub> exhibited excellent optical properties, good

<sup>\*</sup> Corresponding author. E-mail address: xiaoyanlithu@tsinghua.edu.cn (X. Li).

mechanical stability and flexibility [14]. However, it remains challenging to fabricate the fully dense and defect-free nanocrystalline TiO<sub>2</sub> by compressing nanoparticles [12,13]. The defects (such as voids and interfaces) [12] generated during processing have significant influence on the mechanical properties of fabricated nanocrystalline TiO2. Recently, Wang et al. used a blowspinning solution to fabricate TiO<sub>2</sub> nanofibers with a mean grain size below 10 nm, while simultaneously collecting the nanofibers ejected during blow-spinning through an air-permeable cage-like collector [15]. As a result, a large number of TiO<sub>2</sub> nanofibers tangled together to form a three-dimensional (3D) highly porous sponge [15]. In situ mechanical testing showed that such nanofiber sponges exhibited excellent resilience at both room temperature and high temperatures of 400–800 °C [15]. The resilience of these TiO<sub>2</sub> nanofiber sponges is associated with the high porosity of the overall structure and the microstructures (such as diameter and grain size) of the constituent nanofibers. More detailed experimental studies indicated that as the grain size of nanofibers decreased, the nanofiber sponges became more resilient and deformable [15].

In nature, TiO<sub>2</sub> exists in three different phases, namely, anatase, rutile and brookite [16]. The rutile phase is generally used as a white pigment and opacifier [16], while the brookite phase is not used commercially due to its relatively rare reserves [16]. In recent years, nanocrystalline anatase has been widely applied in solar cells and photocatalysts [1,2,14]. Therefore, the photovoltaic and photocatalytic properties of nanocrystalline anatase have been extensively studied. Mechanical behaviors and properties of nanocrystalline anatase are crucial for its industrial applications. However, there have been only a few limited studies on these issues. These studies mainly focused on the elastic properties and phase transition of nanocrystalline anatase under extreme hydrostatic pressure conditions [16-20]. It was experimentally discovered that the bulk modulus of nanocrystalline anatase depends on the grain size [17]. More interestingly, a few experimental and computational studies [18-20] showed that the application of high pressure can induce a phase transition of nanocrystalline anatase that also shows a significant dependence on the grain size. When the grain size is below 10 nm, nanocrystalline anatase transforms to the amorphous phase at high pressure [18]. Nanocrystalline anatase with a grain size of 12-50 nm transforms to the monoclinic baddeleyite-structured phase under the pressure of 12-20 GPa and then transforms into the TiO2-II structure during further decompression [18]. Nanocrystalline anatase with a grain size above 50 nm directly transforms to the  $TiO_2$ -II structure at pressures beyond 5 GPa [18]. However, to date, there have been few studies on the mechanical deformation of nanocrystalline anatase under common mechanical loading. Thus, a fundamental understanding of the deformation mechanisms of nanocrystalline anatase is currently lacking. In this paper, we investigated the deformation of nanocrystalline anatase with a mean grain size of 2-6 nm under uniaxial tension and compression by using large-scale atomistic simulations. Our simulation results showed superplasticity and amorphization of nanocrystalline anatase under uniaxial tension and compression, respectively. Our results further revealed the underlying deformation mechanisms responsible for the superplasticity and amorphization, as well as the influence of the grain size on the deformation behaviors and mechanisms. These results provide an insightful understanding of the plastic deformation of nanocrystalline anatase, as well as a guide for applications of nanocrystalline anatase.

#### 2. Materials and methods

To investigate the mechanical behaviors and properties of nanocrystalline TiO<sub>2</sub> anatase, we carried out a series of large-scale molecular dynamics (MD) simulations using the large-scale

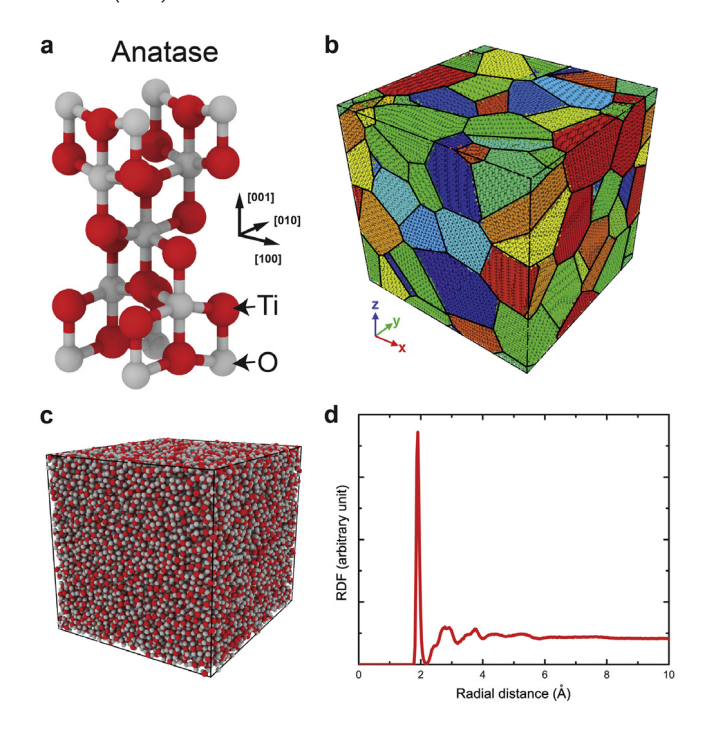


**Fig. 1.** (a) Atomic configuration of anatase unit cell. Ti and O atoms are shown in red and silver, respectively. (b) Atomic configuration of typical nanocrystalline anatase TiO<sub>2</sub> with mean grain size of 6 nm. (c) Atomic configuration of amorphous TiO<sub>2</sub>. (d) RDF of amorphous TiO<sub>2</sub>.

atomistic/molecular massively parallel simulator (LAMMPS) [21]. The anatase unit cell is shown in Fig. 1(a). Two types of simulated samples were used: the first is the nanocrystalline cubic sample with 64 grains (Fig. 1(b)) (with dimensions of  $24 \times 24 \times 24 \times 8 \times 8 \times 8$ nm<sup>3</sup>), and the second is an amorphous cubic sample with dimensions of  $8 \times 8 \times 8$  nm<sup>3</sup>. The largest sample contains 1,680,400 atoms. For nanocrystalline samples, polycrystalline configurations were generated according to the Voronoi method [22]. The mean grain size of the nanocrystalline sample varies from 2 nm to 6 nm, but the grain shape and orientation remain the same for different nanocrystalline samples. The amorphous sample was generated by a melting-and-quenching process reported previously [23]. During this process, the temperature was controlled to increase from 1 K to 2500 K within 200 ps, then remained at 2500 K for 100 ps, finally decreasing to 300 K within 400 ps. The amorphous sample can be regarded as a limiting case, i.e., a nanocrystalline sample with a mean grain size approaching atomic size. Fig. 1(c) shows the atomic configuration of the amorphous sample after equilibration. Its corresponding radial distribution function (RDF) is shown in Fig. 1(d), indicating the amorphous structure. During our simulations, the time step for integration was set as 1 fs. All simulated samples were initially equilibrated by energy minimization, then freely relaxed for 100 ps, and then stretched or compressed along the z-axis under a constant strain rate of  $5 \times 10^8$  s<sup>-1</sup>. During free relaxation, the temperature was kept at 300 K, and the pressures in all three directions were controlled to be zero via a NPT ensemble [24]. During loading, the temperature remained at 300 K, and the pressures along the two non-loading directions were set to zero via the NPT ensemble [24]. Throughout the simulations, periodic boundary conditions were imposed on all three directions of the simulated samples.

To date, several interatomic potentials have been developed for TiO<sub>2</sub> [25–30]. Of these potentials, the pairwise potential proposed by Matsui and Akaogi (MA) [27] and the variable charge potential proposed by Swamy and Gale [30] are the most popular potentials

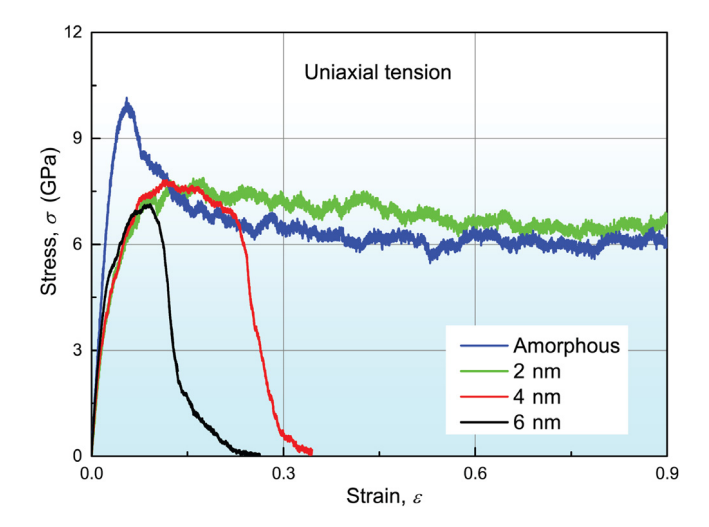


**Fig. 2.** Uniaxial tensile stress–strain curves of nanocrystalline anatase TiO<sub>2</sub> with different grain sizes from MD simulations. The fracture strain significantly increases with the reduction in grain size. The nanocrystalline sample with grain size of 2 nm and the amorphous sample can survive tensile strains over 90%.

and have been widely used for TiO2 in MD simulations. The MA potential is composed of the pairwise additive Coulomb, dispersion and repulsion interactions [27], while the potential developed by Swamy and Gale involves a quantum charge equilibration scheme on the basis of the pairwise Morse potential and is generally referred to as MS-Q potential. This interatomic interaction is described by a transferable variable-charge potential [30] and composed of pairwise Coulomb interactions and non-electrostatic interactions that are subsumed into a two-body Morse potential [30]. Due to its introduction of the quantum charge equilibration scheme, the MS-Q potential is more complicated than the MA potential, so it is computationally much more expensive than the MA potential. The MS-Q potential can reproduce the crystal structures of almost all Ti-O compounds, the elastic properties and relative stability of various TiO2 polymorphs, and the formation energy of the (100) rutile surface [30]. A comprehensive comparison of the MS-Q with the MA potentials has been conducted in the literature [31], with results showing that the MS-Q potential is more successful in predicting the bulk moduli of low-pressure polymorphs (including rutile, anatase, and brookite) than the MA potential. The phase stabilities of both low-pressure and highpressure phase diagrams obtained with the MS-Q potential are in broad agreement with the available calorimetric, phase equilibrium, and other simulation data [31]. Therefore, the MS-Q potential was adopted in the present work to describe the interatomic interaction due to its good accuracy and reliability despite its computational cost.

To further confirm the effectiveness and accuracy of the MS-Q potential, we calculated the elastic properties of nanocrystalline anatase and its compressibility under hydrostatic pressure using the MS-Q potential model. We performed MD simulations for uniaxial tension of nanocrystalline anatase with a mean grain size of 2-6 nm. By fitting the linear regime of uniaxial tensile stress-strain curves, the Young's modulus was obtained as 201.5-169.7 GPa, comparable to experimental nanoindentation measurement (170 GPa) for nanocrystalline anatase thin films with mean grain size of 100-200 nm [32]. We also conducted MD simulations for hydrostatic compression on nanocrystalline anatase with a mean grain size of 4 nm. By fitting the linear part of the hydrostatic stress-volumetric strain curve, the bulk modulus was obtained as 166.2  $\pm$  3.0 GPa, in good agreement with the 165-185 GPa obtained experimentally for nanocrystalline specimens with grain sizes of 4–6 nm [17].

During the simulations, the atomic strains were calculated by a local transformation matrix between the current and reference configurations [33]. The reference configuration is taken as the initial configuration after equilibrium and prior to mechanical loading. The local transformation matrix  $J_i$  of atom i is given by [33],

$$\mathbf{J}_{i} = \left[ \sum_{j \in N_{i}^{0}} \left( \mathbf{d}_{ji}^{0} \right)^{T} \mathbf{d}_{ji}^{0} \right]^{-1} \left[ \sum_{j \in N_{i}^{0}} \left( \mathbf{d}_{ji}^{0} \right)^{T} \mathbf{d}_{ji} \right]$$

$$(1)$$

where  $\mathbf{d}_{ji}^0$  and  $\mathbf{d}_{ji}$  represent the vector separation between atom j and i of the reference and current configurations, respectively, j is one of the nearest neighbors of atom i and  $N_i^0$  is the total number of nearest neighbors of atom i at the reference configuration. For each  $\mathbf{J}_i$ , the local Lagrangian strain tensor  $\eta_i$  (i.e atomic strain tensor) is calculated as [33],

$$\eta_i = \frac{1}{2} \left[ \mathbf{J}_i (\mathbf{J}_i)^T - \mathbf{I} \right] \tag{2}$$

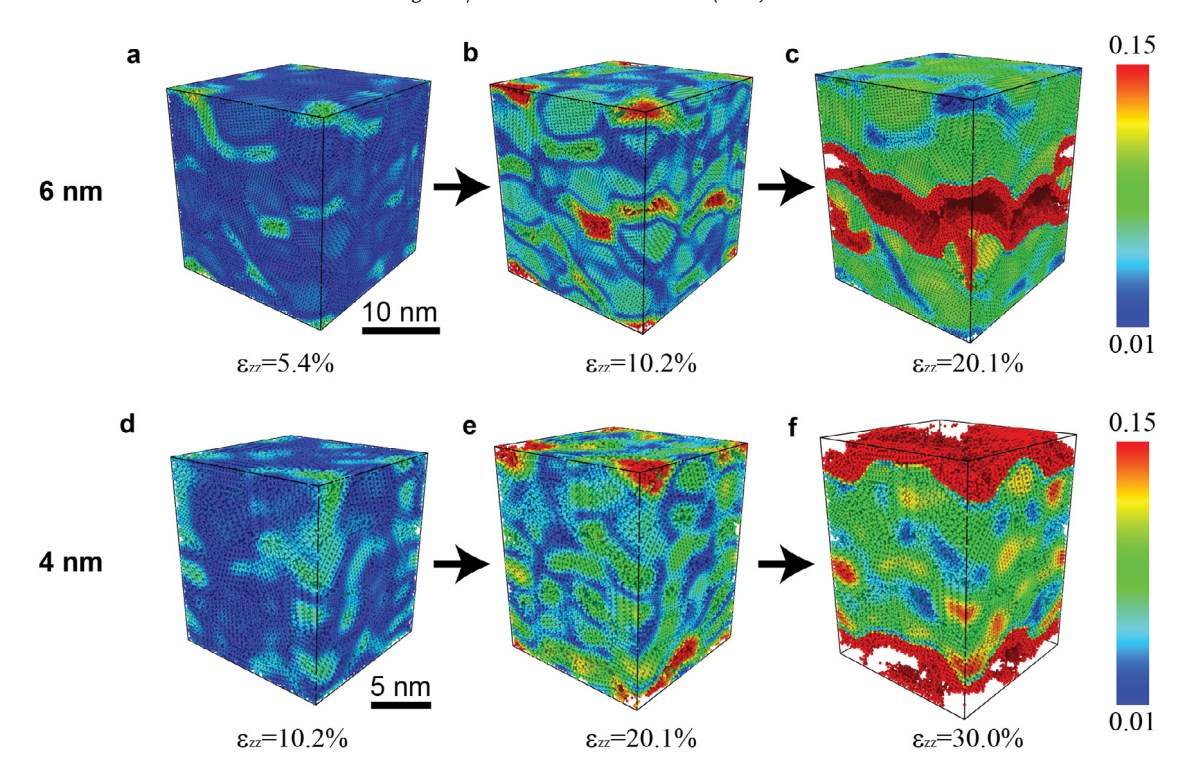
where I is the unit tensor. Such method for calculation of atomic strains has been widely used to characterize the large plastic deformation of various amorphous and crystalline nanostructured materials [34–37]. The atomic stresses were calculated based on the Virial theorem. The stress of the overall sample was taken as the average over the atomic stresses of all atoms in the sample.

#### 3. Results and discussion

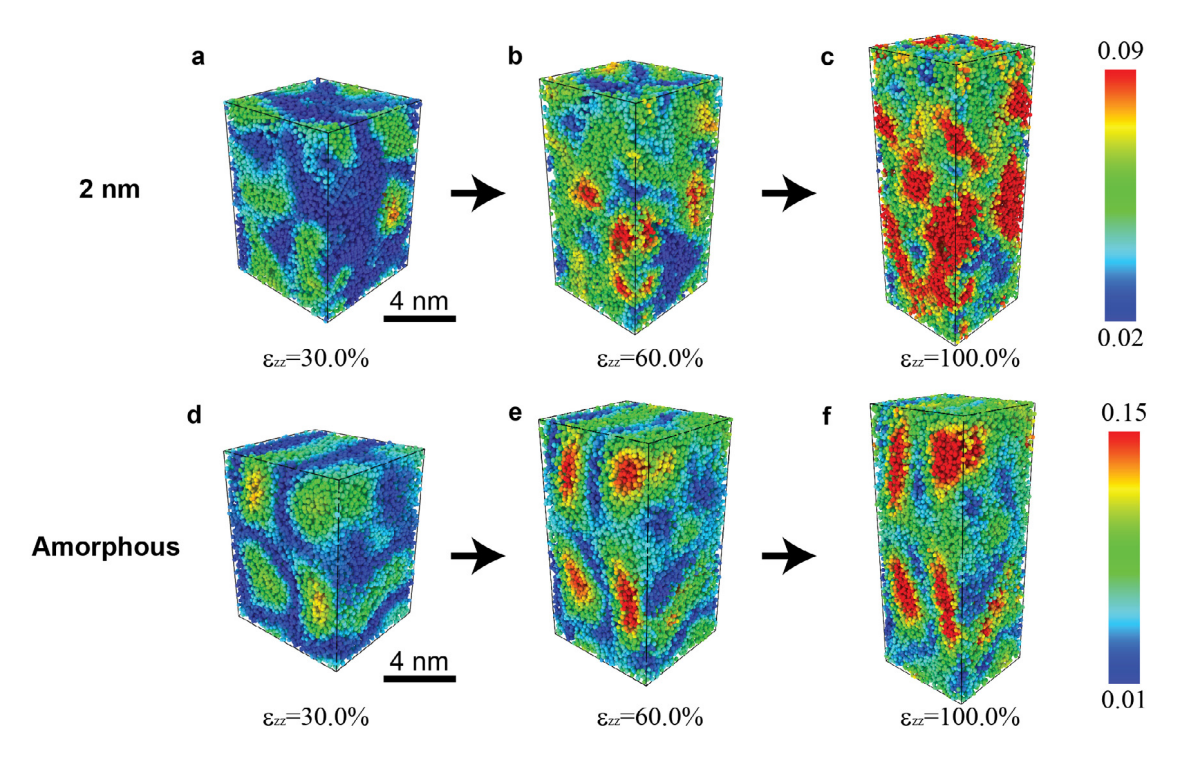
#### 3.1. Superplasticity of nanocrystalline TiO<sub>2</sub> under uniaxial tension

Fig. 2 shows the uniaxial tensile stress-strain curves for nanocrystalline anatase with mean grain sizes of 2-6 nm and for amorphous TiO<sub>2</sub>. It can be seen from these stress-strain curves that with the increase in applied strain, all samples first underwent a linear elastic deformation with  $\sim$ 3% strain, followed by a plastic hardening regime where the stress continuously increased up to a maximum. Subsequently, the stresses of the nanocrystalline samples (with grain sizes of 4 nm and 6 nm) rapidly dropped to zero so that their fracture strains were only approximately 30%. However, the stresses of the sample with a grain size of 2 nm and the amorphous sample gradually saturated to a constant level after 20% tensile strain. These two samples were stretched into 90% strain without fracture, indicating a superplastic deformation at room temperature. These simulation results showed that as the grain size decreases, the fracture strain (or elongation) of the nanocrystalline samples increases significantly and that there exists a brittle-to-ductile transition for the grain sizes in the range of 2-4 nm. It is noted that the maximum tensile stress of the amorphous sample is higher than that of the nanocrystalline samples. This is related to the apparent stress overshooting of the amorphous sample shown in Fig. 2, which originates from delayed free volume activation for plastic deformation in amorphous materials [38].

Fig. 3 depicts a sequence of snapshots of stretched nanocrystalline anatase with grain sizes of 4 nm and 6 nm at different tensile strains. At the initial stage, large shear strains were primarily localized at the grain boundaries (GBs) due to local stress concentrations, as shown in Fig. 3(a) and (d). As the applied strain increased, several nanocracks nucleated at the GBs (Fig. 3(b) and (e), and then propagated along the GBs and merged into an interconnected channel in the direction normal to the tensile direction, eventually resulting in inter-granular brittle fracture (Fig. 3(c) and (f)). Thus, the fracture strains (or elongations) of the samples with grain sizes of 6 nm and 4 nm are only approximately 20% and 30%, respectively. Movie 1 shows the evolution of a nanocrystalline sample with a grain size of 6 nm under uniaxial tension.



**Fig. 3.** (a)–(c) Atomic configurations of the sample with a grain size of 6 nm under different tensile strains. (d)–(f) Atomic configurations of the sample with a grain size of 4 nm under different tensile strains. During deformation of these two samples, a few nano-cracks nucleate at GBs and then merge into larger cracks, leading to brittle intergranular fracture of samples at higher strains. All atoms are colored based on their atomic von Mises strains.



**Fig. 4.** (a)–(c) Atomic configurations of the sample with a grain size of 2 nm under different tensile strains. (d)–(f) Atomic configurations of the amorphous sample under different tensile strains. As the grain size is reduced to 2 nm, GB sliding and nano-cavitation exert an effect during tensile deformation, resulting in fracture strain beyond 90%. For the amorphous sample, nano-cavitation serves as the dominant deformation mechanism, also showing fracture strain greater than 90%. All atoms are colored according to their atomic von Mises strains.

For the nanocrystalline sample with a grain size of 2 nm, large shear strains were still initially distributed at the GBs, as shown in Fig. 4(a). Compared to the samples with larger grain sizes, the sample with a grain size of 2 nm has a much larger GB fraction. As a result, the shear strain distribution in the sample with a

grain size of 2 nm is relatively uniform. As the applied strain increased, the shear strain accumulated around the GBs. When the applied strain reached 30%, the samples with grain sizes of 4–6 nm failed due to intergranular fracture (Fig. 3(c) and (f), but no crack nucleation occurred in the sample with a grain size of 2 nm. The

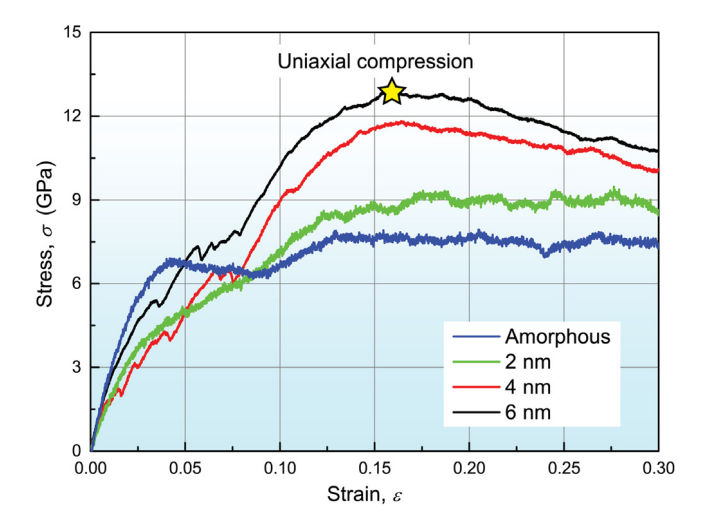


**Fig. 5.** Uniaxial compressive stress-strain curves of nanocrystalline TiO<sub>2</sub> with different grain sizes from MD simulations.

accumulation of the shear strain at GBs indicated the activation of GB sliding [39,40]. As the strain increased further, some nanoscale cavities nucleated, as illustrated by Fig. 4(a) and (b). These nanocavities were distributed uniformly throughout the whole sample instead of coalescing into nano-cracks, as shown in Fig. 4(c). Such nano-cavitation contributes to a stable plastic flow and therefore facilitates the improvement in the ductility of the nanocrystalline sample. Similar nano-cavitation has also been reported in recent MD simulations of superplastic deformation of nanocrystalline SiC with a grain size of 2 nm [11]. For the nanocrystalline sample with a grain size of 2 nm, GB sliding and nano-cavitation result in superplastic deformation under tension. More details of this process are shown in Movie 2. For the amorphous sample,

nano-cavitation serves as the dominant deformation mechanism, leading to a fracture strain higher than 90%, as evidenced by Fig. 4(d)–(f). In amorphous materials, nucleation of nanoscale cavities is usually related to free volume activation. In addition to nanocavitation, it was observed that some atom clusters experienced large shear strains, as shown in Fig. 4(e). For the stress–strain curves shown in Fig. 2, the amorphous sample shows a more apparent strain softening (i.e., stress drop) than the nanocrystalline samples after reaching maximum stress, which is attributed to a complex interaction between the shear of the atom cluster and the nano-cavitation [38].

# 3.2. Amorphization of nanocrystalline $TiO_2$ under uniaxial compression

Fig. 5 show the uniaxial compressive stress–strain curves for nanocrystalline samples with grain sizes of 2–6 nm and for the amorphous sample. After the linear elastic deformation, all samples underwent pronounced plastic deformation. For nanocrystalline samples with grain sizes of 4 and 6 nm, the stress first increased to a peak value, indicating strain hardening, and then decreased slightly. However, for the nanocrystalline sample with a grain size of 2 nm and for the amorphous sample, the stress saturated to a plateau after the plastic yielding. All samples were compressed to 30% strain without failure, indicating good compressibility whose origin is further explored below.

Fig. 6(a) and (b) show the atomic compressive strain  $\varepsilon_{zz}$  and stress  $\sigma_{zz}$  contours of the nanocrystalline sample with a grain size of 6 nm at the applied strain of 15.9%. To eliminate the effects of thermal fluctuations, the atomic stress of each atom in Fig. 6(b) is obtained as an average over all atoms in a sphere with a radius of 1 nm centered at this atom. It was found that within regions with high compressive strains, there were many disordered atoms distributed along the GBs, as indicated by the black lines in Fig. 6(a). We further examined the atomic configurations of two sites near GBs at compressive strains of 0 and 15.9%. It can be seen in Fig. 6(c)

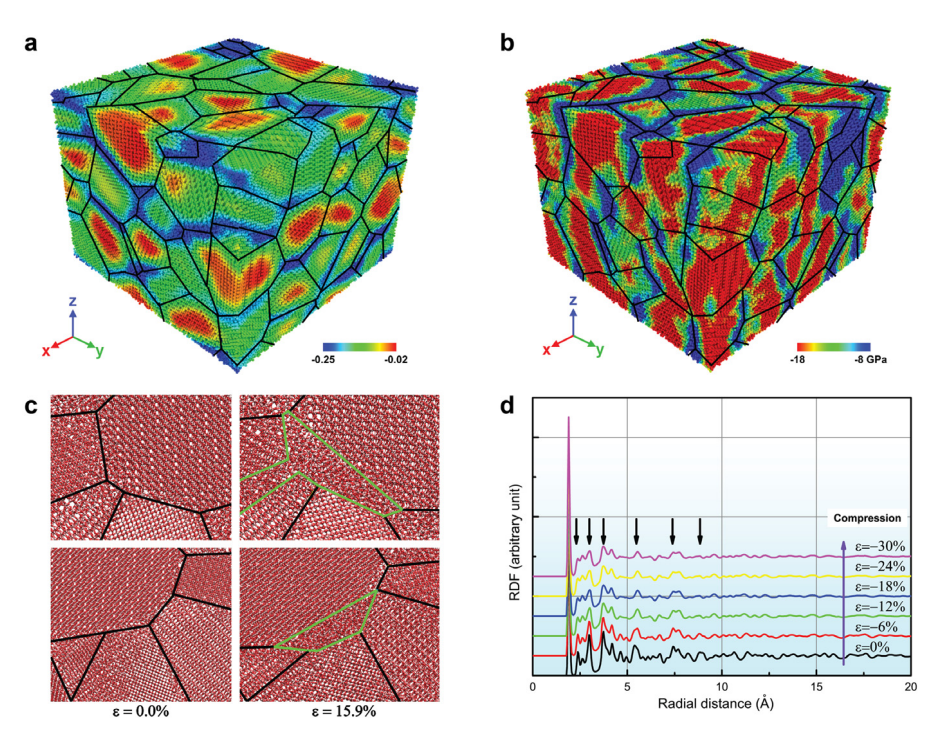


**Fig. 6.** (a,b) Atomic compressive strain and stress contours of nanocrystalline anatase with grain size of 6 nm at an applied strain of 15.9%. GBs are indicated by the black lines. (c) Atomic configurations of two specific sites of nanocrystalline anatase at compressive strains of 0% and 15.9%, demonstrating that crystalline-to-amorphous transition initiates from GBs. GBs are indicated by the black lines, while the regions outlined by the green lines contain the amorphous phase after transition. (d) RDF curves of nanocrystalline anatase with a grain size of 6 nm during uniaxial compression.

that the crystal lattices near the GBs (as marked by green lines) transformed into completely disordered structures after the compression. These results suggest that a crystalline-to-amorphous transition (i.e., amorphization) of anatase was initiated from GBs during the compression. Fig. 6(d) shows the RDFs of the nanocrystalline sample with a grain size of 6 nm at different compressive strains. The intensity of peaks attenuates as the compressive strain increases. Notably, some of the peaks reflecting long-range order even disappear at higher strain levels (marked by black arrows in Fig. 6(d)), further demonstrating the occurrence of amorphization under large compression. Previous experimental studies [18-20] have shown that when the grain size is below 10 nm, nanocrystalline anatase can transform into the amorphous phase at a high pressure of 10-25 GPa. As shown in Fig. 6(b), local compressive stresses in the nanocrystalline sample are usually as high as 18 GPa, consistent with previous experimental measurements of the critical pressure (10–25 GPa) for amorphization. This indicated that the amorphization observed in the nanocrystalline samples is induced by the high compressive stress. It is noted in Fig. 6(b) that because the regions near GBs have transformed into the amorphous phase, high local compressive stresses are mainly distributed in the grain interiors. This implies that high local compressive stresses extended from GBs into grain interiors, leading to an extension of amorphization from the GBs to grain interiors. A compression process of the nanocrystalline sample with a grain size of 6 nm is shown in detail in Movie 3. At the initial stage of compression, high compressive strain/stress initially localized at the GBs composed of disordered atoms. When the local compressive stresses near the GBs reach a critical value, high local stresses gradually drive the crystalline-to-amorphous transformation. As the applied strain increased, the amorphous regions gradually extended from the GBs to grain interiors. High compressive strains always localized on the transformed amorphous phases, contributing to the plastic flow and compressibility of the overall sample as observed in the stressstrain curves presented in Fig. 5.

Our MD simulations provided the mechanistic details of the plastic deformation of nanocrystalline anatase under tension and compression. During tension, high shear strains mainly localized at the GBs, leading to the occurrence of sliding and nanocavitation near the GBs. During compression, high compressive strains/stresses were initially generated near the GBs, initiating amorphization from the GBs. These results indicated that in nanocrystalline samples, GBs play an important role in uniaxial tensile and compressive deformation. In nanocrystalline materials, GBs are usually regarded as disordered structures (similar to the amorphous phase), compared to the grain interior with ordered lattices [39,41]. Our MD simulations showed that the amorphous sample can sustain larger fracture strain than the nanocrystalline samples under both tension and compression. Therefore, in the nanocrystalline samples, GBs with disordered structures bear large strains during both tension and compression, which is also evidenced by Figs. 3, 4 and 6(a)–(b). Based on a previous theoretical model [41], if the GB thickness is set as 0.75 nm, the volume fraction of the GBs of the nanocrystalline samples increases from 30% to 71%, as the grain size is reduced from 6 nm to 2 nm. This implies that as the grain size decreases, GB-related processes such as GB sliding, nano-cavitation and amorphization become more dominant during the deformation, leading to the tensile superplasticity and good compressibility of the nanocrystalline samples.

Our MD simulations showed that in contrast to nanocrystalline anatase phases, amorphous phases have comparable strength and better deformability under both tension and compression. These differences in mechanical properties between nanocrystalline and amorphous TiO<sub>2</sub> are attributed to their distinct difference in the microstructure. Due to the better mechanical properties/performance, amorphous TiO<sub>2</sub> might have a wider application

in optical coatings and mixed conductors. Moreover, it is noted that the critical stress for amorphization of nanocrystalline  ${\rm TiO_2}$  from our MD simulations is relatively higher than that from experimental measurements [18–20], and their fracture strain from MD simulations is relatively large. These differences are mainly attributed to a fact that our MD simulations used much higher strain rate than experiments. It might be also associated with the accuracy of the interatomic potential used for modeling large deformation and fracture, which involve some critical events, such as the breakage and formation of ionic bonds and the occurrence of multiple oxide states. The current empirical potential cannot capture these critical events as accurate as ab-initio calculations [30].

#### 4. Conclusions

In summary, we have studied the tensile and compressive deformations of nanocrystalline anatase TiO2 using large-scale MD simulations. Our MD simulations showed that during uniaxial tension, nanocrystalline samples with a grain size of 2 nm underwent superplastic deformation, leading to a fracture strain greater than 90%. During uniaxial compression, nanocrystalline samples exhibited good compressibility. Our simulations further revealed that the observed tensile superplasticity is attributed to the dominance of GB sliding and nano-cavitation during the deformation. while the good compressibility is associated with amorphization induced by high compressive stress. These unique tensile and compressive behaviors are related to high volume fractions of GBs with disordered structures, which can accommodate large strains during both tension and compression. Our current work provides a fundamental understanding of plastic deformation of nanocrystalline anatase TiO<sub>2</sub>, as well as mechanistic insights into the enhancement of the tensile and compressive deformability of ceramics by refining the grains.

#### Acknowledgments

X.L. gratefully acknowledges financial support from the National Natural Science Foundation of China (Grant Nos. 11522218 and 11720101002), the National Basic Research of China (Grant No. 2015CB932500), and the Chinese 1000-Talents Plan for Young Researchers. H.G. acknowledges funding from the National Science Foundation (Grant No. DMR-1709318). The simulations were performed on the TianHe-1 supercomputer at the National Supercomputer Center in Tianjin.

### Appendix A. Supplementary data

Supplementary material related to this article can be found online at https://doi.org/10.1016/j.eml.2018.05.009.

#### References

- Z. Zhang, C.C. Wang, R. Zakaria, J.Y. Ying, Role of particle size in nanocrystalline TiO<sub>2</sub>-based photocatalysts, J. Phys. Chem. B 102 (1998) 10871–10878.
- [2] H. Lin, C.P. Huang, W. Li, C. Ni, S.I. Shah, Y.H. Tseng, Size dependency of nanocrystalline TiO<sub>2</sub> on its optical property and photocatalytic reactivity exemplified by 2-chlorophenol, Appl. Catal. B 68 (2006) 1–11.
- [3] J. Karch, R. Birringer, H. Gleiter, Ceramics ductile at low temperature, Nature 330 (1987) 556–558.
- [4] Y. Maehara, T.G. Landon, Superplasticity in ceramics, J. Mater. Sci. 25 (1990) 2275–2286.
- [5] A. Lai, Z. Du, C.L. Gan, C.A. Schuh, Shape memory and superelastic ceramics at small scales, Science 341 (2013) 1505–1508.
- [6] B.R. Lawn, N.P. Padture, H. Cai, F. Guiberteau, Making ceramics "ductile", Science 263 (1994) 1114–1117.
- [7] T.G. Nieh, J. Wadsworth, Superelastic behaviour of a fine-grained, yttriastabilized, tetragonal zirconia polycrystal (Y-TZP), Acta. Metall. Mater. 38 (1990) 1121–1133.

- [8] P. Gruffel, P. Carry, A. Mocellin, Effect of testing conditions and doping on superplastic creep of alumina, Rev. Phys. Appl. 23 (1988) 716–716.
- [9] F. Wakai, Y. Kodama, S. Sakaguchi, T. Nonami, Superplasticity of hot isostatically pressed hydroxyapatite, J. Am. Ceram. Soc. 73 (1990) 457–460.
- [10] B.N. Kim, K. Hiraga, K. Morita, Y. Sakka, A high-strain-rate superplastic ceramic, Nature 413 (2001) 288–291.
- [11] J.Y. Zhang, Z.D. Sha, P.S. Branicio, Y.W. Zhang, V. Sorkin, Q.X. Pei, D.J. Srolovitz, Superplastic nanocrystalline ceramics at room temperature and high strain rates, Scr. Mater. 69 (2013) 525–528.
- [12] D. Li, Y. Xia, Fabrication of titania nanofibers by electrospinning, Nano Lett. 3 (2003) 555–560.
- [13] E.S. Medeiros, G.M. Glenn, A.P. Klamczynski, W.J. Orts, L.H.C. Mattoso, Solution blowspinning: A new method to produce micro- and nanofibers from polymer solutions, J. Appl. Polym. Sci. 113 (2009) 2322–2330.
- [14] D. Zhang, J.A. Downing, F.J. Knorr, J.L. McHale, Room-temperature preparation of nanocrystalline TiO<sub>2</sub> films and the influence of surface properties on dyesensitized solar energy conversion, J. Phys. Chem. B 110 (2006) 21890–21898.
- [15] H. Wang, X. Zhang, N. Wang, Y. Li, X. Feng, Y. Huang, C. Zhao, Z. Liu, M. Fang, G. Ou, H. Gao, X. Li, H. Wu, Ultralight, scalable, and high-temperature-resilient ceramic nanofiber sponges, Sci. Adv. 3 (2017) e1603170.
- [16] J. Muscat, V. Swamy, N.M. Harrison, First-principles calculations of the phase stability of TiO<sub>2</sub>, Phys. Rev. B 65 (2002) 224112.
- [17] Y. Al-Khatatbeh, K.K.M. Lee, B. Kiefer, Compressibility of nanocrystalline TiO<sub>2</sub> anatase, J. Phys. Chem. C 116 (2012) 21635–21639.
- [18] V. Swamy, A. Kuznetsov, L.S. Dubrovinsky, R.A. Caruso, D.G. Shchukin, B.C. Muddle, Finite-size and pressure effects on the Raman spectrum of nanocrystalline anatase TiO<sub>2</sub>, Phys. Rev. B 71 (2005) 184302.
- [19] V. Swamy, A. Kuznetsov, L.S. Dubrovinsky, P.F. McMillan, V.B. Prakapenka, G. Shen, B.C. Muddle, Size-dependent pressure-induced amorphization in pagescale TiO<sub>2</sub>, Phys. Rev. Lett. 96 (2006) 135702
- [20] V. Pischedda, G.R. Hearne, A.M. Dawe, J.E. Lowther, Ultrastability and enhanced stiffness of ~6 nm TiO₂ nanoanatase and eventual pressure-induced disorder on the nanometer scale, Phys. Rev. Lett. 96 (2006) 035509.
- [21] S. Plimpton, Fast parallel algorithms for short-range molecular dynamics, J. Comput. Phys. 117 (1995) 1–19.
- [22] G. Voronoï, Nouvelles applications des paramètres continus à la théorie des formes quadratiques, J. Reine Angew. Math. 134 (1908) 198–287.
- [23] B. Ding, X. Li, X. Zhang, H. Wu, Z. Xu, H. Gao, Brittle versus ductile fracture mechanism transition in amorphous lithiated silicon: From intrinsic nanoscale cavitation to shear banding, Nano Energy 18 (2015) 89–96.
- [24] M. Parrinello, A. Rahman, Polymorphic transitions in single crystals: A new molecular dynamics method, J. Appl. Phys. 52 (1981) 7182–7190.

- [25] G.V. Lewis, C.R.A. Catlow, Potential models for ionic oxides, J. Phys. C Solid State 18 (1985) 1149.
- [26] M. Mostoller, J.C. Wang, Ionic potential models in insulators having the rutile structure, Phys. Rev. B 32 (1985) 6773.
- [27] M. Matsui, M. Akaogi, Molecular dynamics simulation of the structural and physical properties of the four polymorphs of TiO<sub>2</sub>, Mol. Simul. 6 (1991) 239– 244
- [28] D.W. Kim, N. Enomoto, Z.E. Nakagawa, K. Kawamura, Molecular dynamic simulation in titanium dioxide polymorphs: Rutile, brookite, and anatase, J. Am. Ceram. Soc. 79 (1996) 1095–1099.
- [29] S. Ogata, H. Iyetomi, K. Tsuruta, F. Shimojo, R.K. Kalia, A. Nakano, P. Vashishta, Variable-charge interatomic potentials for molecular-dynamics simulations of TiO<sub>2</sub>, J. Appl. Phys. 86 (1999) 3036–3041.
- [30] V. Swamy, J.D. Gale, Transferable variable-charge interatomic potential for atomistic simulation of titanium oxides, Phys. Rev. B 62 (2000) 5406.
- [31] V. Swamy, J.D. Gale, L.S. Dubrovinsky, Atomistic simulation of the crystal structures and bulk moduli of TiO<sub>2</sub> polymorphs, J. Phys. Chem. Solids 62 (2001) 887–895
- [32] O. Zywitzki, T. Modes, H. Sahm, P. Frach, K. Goedicke, D. Glöß, Structure and properties of crystalline titanium oxide layers deposited by reactive pulse magnetron sputtering, Surf. Coating. Tech. 180 (2004) 538–543.
- [33] F. Shimizu1, S. Ogata, J. Li, Theory of shear banding in metallic glasses and molecular dynamics calculations, Mater. Trans. 48 (2007) 2923–2927.
- [34] A. Cao, Y. Cheng, E. Ma, Structural processes that initiate shear localization in metallic glass, Acta Mater. 57 (2009) 5146–5155.
- [35] L. Zhang, Y. Cheng, A. Cao, J. Xu, E. Ma, Bulk metallic glasses with large plasticity: Composition design from the structural perspective, Acta Mater. 57 (2009) 1154–1164.
- [36] C. Deng, F. Sansoz, Enabling ultrahigh plastic flow and work hardening in twinned gold nanowires. Nano Lett. 9 (2009) 1517–1522.
- [37] H. Zhou, X. Li, Y. Wang, Z. Liu, W. Yang, H. Gao, Torsional detwinning domino in nanotwinned one-dimensional nanostructures, Nano Lett. 15 (2015) 6082– 6087
- [38] M. Jiang, G. Wilde, L. Dai, Origin of stress overshoot in amorphous solids, Mech. Mater. 81 (2015) 72–83.
- [39] Y. Wei, L. Anand, Grain-boundary sliding and separation in polycrystalline metals: application to nanocrystalline fcc metals, J. Mech. Phys. Solids 52 (2004) 2587–2616.
- [40] T. Zhu, J. Li, Ultra-strength materials, Prog. Mater. Sci. 55 (2010) 710-757.
- [41] M.A. Meyers, A. Mishra, D.J. Benson, Mechanical properties of nanocrystalline materials, Prog. Mater. Sci. 51 (2006) 427–556.